Journal of Environmental Chemical Engineering 10 (2022) 107648

Contents lists available at ScienceDirect

Journal of Environmental Chemical Engineering

journal homepage: www.elsevier.com/locate/jece

Effect of pore size and electrolyte flow rate on the bubble removal efficiency of 3D pure Ni foam electrodes during alkaline water electrolysis

Fernando Rocha, Renaud Delmelle, Christos Georgiadis, Joris Proost *

Division of Materials and Process Engineering, Université catholique de Louvain, Place Sainte-Barbe 2, B-1348 Louvain-la-Neuve, Belgium

ARTICLE INFO

Editor: Despo Kassinos

Keywords:
Alkaline water electrolysis
Bubble removal
Nickel foam
Pore size
Process intensification

ABSTRACT

To further reduce the capital expenditure of alkaline water electrolyzers, an improvement in power density can still be achieved through process intensification. The change from traditional gap-cells to zero-gap cells has already been proven to be very promising in this respect. In the zero-gap design, macro-porous 3D structures are typically being used as electrodes. Here, pure nickel foams with different pore sizes in the range 450 – 3000 μm have been studied under well-controlled electrolyte flow conditions. To this end, a dedicated flow cell has first been constructed that allows for imposing the same relatively high flow rates on the order of 1 L/min that are typically encountered under industrial conditions. Our specific cell design was shown by computational fluid dynamic simulations to be able to homogenize the flow field before entering the electrodes. This is absolutely mandatory to reliably evaluate the intrinsic bubble removal efficiency of the differently sized foams. We then demonstrate that the effect of pore size and the electrochemical performance can be rationalized by considering the cell voltage as a function of electrochemical current density, i.e. the current divided by the theoretically available electrochemical surface area (ECSA) rather than by the projected electrode area. Based on this analysis, we were also able to quantify the bubble removal efficiency by estimating the effective fraction of the ECSA that is not impeded by bubble coverage.

1. Introduction

Reduction of the anthropic impact on our environment requires an in-depth transformation of the global energy grid by increasingly relying on renewable sources. The electricity generated by such sources cannot be effectively stored and transported without converting it to chemical energy, which implies the synthesis, storage and transport of energy carriers. Whether the latter are synthetic hydrocarbons – following the so-called Power-to-Gas strategy [1] – or directly hydrogen – according to so-called hydrogen society models [2] –, production of green hydrogen by water electrolysis remains the crucial link between electricity and chemical energy. Although this technology is known for more than a century [3], the improvement of its performance is still a major research topic.

Nowadays, three main technologies are used to produce hydrogen electrolytically depending on the electrolyte [4,5]: alkaline water electrolysis (AWE), proton exchange membrane (PEM) electrolysis, and solid oxide water electrolysis (SOE). The first one uses an alkaline solution, generally KOH between 1 and 6 M at a temperature in the range 30–80 °C, a diaphragm or an anion exchange membrane, and Ni-based electrodes. The second uses perflurinated polysulfonated membranes, acid electrolytes such as perfluorosulfonic acid, a temperature between 20 and 80 °C and noble metals as catalysts e.g. Pt, Pd, Ir and Ru. The last one consists in the use of solid oxides electrolytes in which O^{2-} is the electron carrier and elevated temperatures between 500 and 1000 °C. AWE is the most mature technology, and it is already used for industrial purposes. The challenge of this technology is the improvement of efficiency and the reduction of the capital expenditure (CAPEX) of electrolyzers. Initially, alkaline electrolyzers used gap-cells, where there was an important physical distance between the cathode and the anode (>2 mm) [6], with a cell separator (membrane or diaphragm) between them. The problem with this configuration is that at high current densities (usually higher than 0.45 A/cm^2 [4]), the produced gases form a non-conductive layer over the entire electrode surface, creating a screening effect and limiting the increase in current density. This effect also causes an increase in the gas cross-over across the cell separator, as it favors gas transport in both directions across the diaphragm [4]. Therefore, this design has gradually been substituted by a zero-gap cell.

* Corresponding author.
E-mail address: joris.proost@uclouvain.be (J. Proost).

https://doi.org/10.1016/j.jece.2022.107648
Received 27 December 2021; Received in revised form 2 March 2022; Accepted 30 March 2022
Available online 1 April 2022

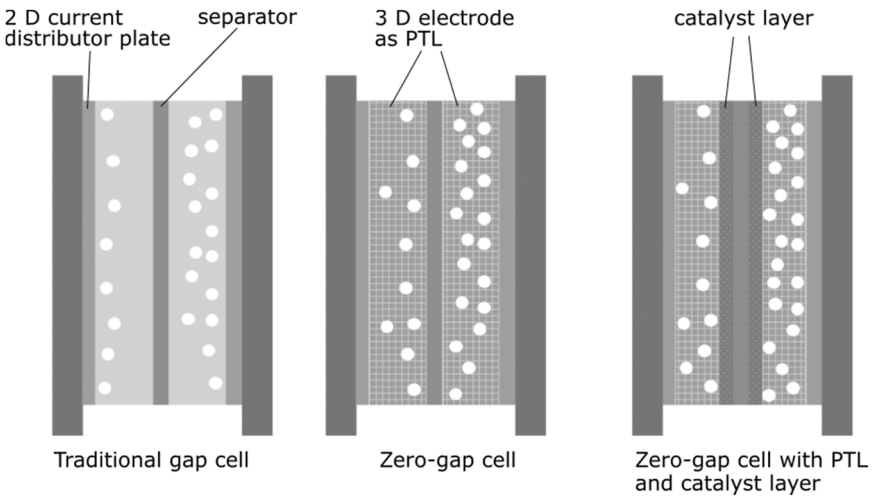

Fig. 1. Different possible cell designs for alkaline water electrolysis (PTL = Porous Transport Layer).

In this case, two additional macro-porous 3D electrodes are compressed to a 2D current distributor plate either side of a membrane or a diaphragm, reducing the electrode distance from a few millimeters to the thickness of the separator. This technology prevents the screening effect and therefore reduces the ohmic losses caused by remaining insulating bubbles in the electrolyte. Furthermore, the reduced interelectrode gap implies a lower electrolyte resistance thus, a lower voltage drop and a more efficient process [6].

The 3D electrodes consist of perforated plates, porous structures, or screen electrodes, allowing hydroxyl ions and gases to pass through. The result is the achievement of current densities of 2 A/cm^2 (at a cell voltage of 1.85 V, 80 °C, 30 wt% KOH, Ni electrodes) [7]. Various strategies leading to improvements in current density – notably optimization of electrode intrinsic activity, resistivity, surface area, bubble removal and stability [8] – means a reduced CAPEX [4] and enables to scale up the electrolyzers to the megawatt level. The different cell designs are shown in Fig. 1. It can be seen that for the traditional cell, gas bubbles evolve from the surface of the 2D current distributor plates only, with an important interelectrode gap. For zero-gap cells, gases may additionally evolve from within the 3D electrode, especially at the region close to the separator, as this is the region with the lowest voltage drop as a consequence of the lower interelectrode distance between the cathode and the anode. Two zero-gap designs are shown. The first one with a porous electrode only and the second one with a porous electrode serving as a porous transport layer (PTL) pressed against a catalyst layer, the latter being either an electrocatalytically coated perforated plate or any other high surface area Ni structure.

An important issue when using the zero-gap configuration is the entrapment of gas bubbles within the 3D electrode, as this will decrease the available surface area and hinder mass transport. The resistance due to bubble coverage is typically the dominant factor at high current densities [8]. With bubbles covering part of the electrode surface, the actual current density j can be expressed in terms of the superficial current density I and the fraction θ of the electrode surface covered by adhering bubbles [6]:

$$j = \frac{I}{1-\theta} \tag{1}$$

In the conventional set-up, the existence of bubbles between the electrodes will also reduce the percentage of the volume which is filled with electrolyte, imposing a resistance in the transport of hydroxyl ions from the cathode to the anode. This will be an issue especially at high current densities, when the percentual volume of bubbles (void fraction) will be significant. The zero-gap solution forces the gas bubbles to be released from the backside of the electrodes, allowing the active side of the electrode (catalyst layer or high surface Ni layer) to be bubble-free. As a result, bubbles will have a smaller contribution to the Ohmic resistance [6]. An important way to effectively remove the produced gases and to feed the electrode surface with electrolytes is the use of a forced electrolyte flow. This solution is particularly important when using foam electrodes and high current densities and can also help in the heat distribution [6]. Another solution to reduce the impact of bubbles is the fabrication of superaerophobic electrode surfaces, which causes a reduction in bubble size and rapid separation from the surface [9].

In the zero-gap configuration, a PTL must be used to ensure electrical contact between the current distributor and the catalyst layer. The PTL needs to ensure efficient gas removal and good electric conductivity. Materials in use nowadays are nickel and stainless steel in the form of metallic meshes, foams, or sintered metals. The focus of the present study will be on metallic foams. Given the stochastic nature of these kinds of PTL, gas bubbles follow a large path until they get out of the electrode. While the fastest path would be to travel upwards, the path of bubbles inside nickel foams will be deviated by the collision with the metallic electrode, presenting a higher residence time. Kou et al. [10] observed that the residence time inside a foam can be significantly higher than the residence time inside a periodic structure, especially when the bubble diameter is large. In their study, no difference in residence time was observed when the bubble diameter was lower than 10 μm. For higher diameters, the residence time of bubbles inside foams may reach 10 times the value obtained for periodic structures. AWE is not the only technology that uses a PTL. In the case of PEM electrolysis, a Ti porous electrode is typically used as PTL [5]. Parra-Restrepo et al. [11] studied different sintered Ti anodes and observed that the pore size and porosity can be optimized to lower the contact resistance with the catalyst layer and to promote an effective gas/water transport.

Alternatively to the use of a catalyst layer, a thin layer of a high surface area pure Ni electrode may be used as well. This approach avoids stability issues related to electrocatalysts. Schalenbach et al. [7] achieved 2 A/cm^2 at 1.92 V, 80 °C, and 30 wt% KOH by increasing a thousand times the surface area of Ni meshes by hot-dip galvanizing in zinc followed by de-alloying. Kim et al. [12] inserted a nickel powder in one side of a nickel foam and sintered it, creating an asymmetrical electrode with a pore size changing from 5 μm at the catalyst layer to 100 μm at the porous transport layer. The current density at 30% KOH, 80 °C, 5 atm, and 1.8 V was close to 0.5 A/cm^2. There are other ways of increasing the surface area of Ni electrodes. Han et al. [13] achieved a 40-fold increase in the surface area using sputtering. As a consequence, at a current density of 0.5 A/cm^2, 25 wt% KOH, 80 °C, Zirfon separator, and Ni foam electrodes, the cell voltage was decreased from 2.2 V to 2.0 V. The authors also compared the performance of a traditional cell

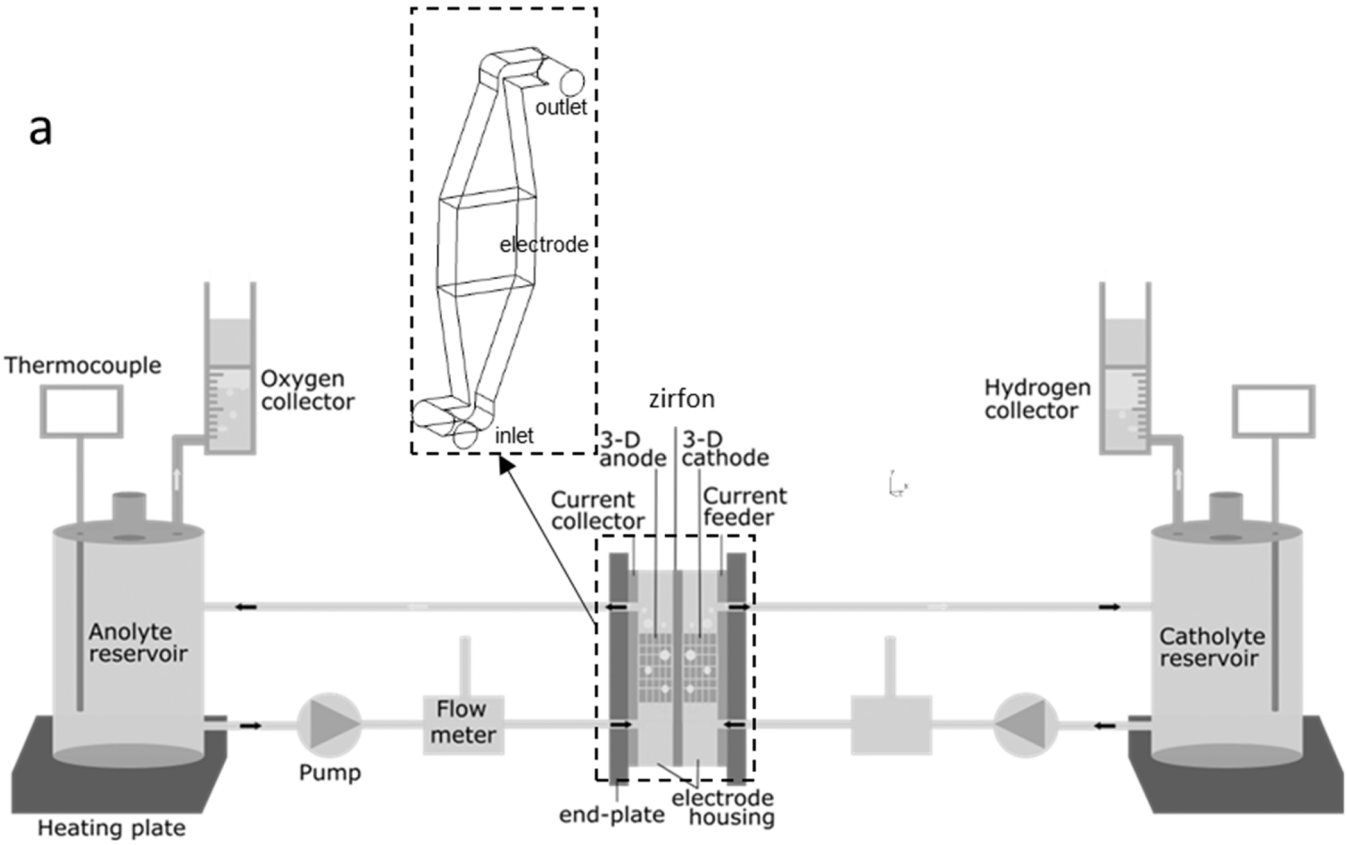

Fig. 2. a) Schematic details of our experimental setup; b) Hydrodynamically optimized cell design with streamlines colored by velocity; c) CFD simulations of velocity profiles at the maximum flow rate of 1.1 L/min for x and y velocity component.

with a zero-gap cell. At the same temperature, electrolyte and separator mentioned previously, the cell voltage for the traditional cell using only bipolar plates was close to 2.40 V at 0.8 A/cm^2, while the value for the zero-gap cell using Ni foams was 2.25 V. Kraglund et al. [14] reduced the cell voltage from 2.1 V to 1.7 V at 0.5 A/cm^2, 24 wt% KOH, 80 °C, Zirfon membrane, by means of vacuum plasma spraying. The cathode was Ni foam and the anode was a Ni perforated plate. It is worth noting that an increase in the ECSA will also cause an increase in bubble generation and coverage, making it difficult to maintain the effective ECSA in the course of water electrolysis. It is then critical to promote an efficient bubble removal [8].

Finally, imposing a forced electrolytic flow is known to cause a reduction in the cell voltage in a traditional AWE gap-cell [15,16], especially when the electrode-membrane gap is lower than 4 mm [17]. A positive effect caused by a forced electrolyte flow was reported as well when using Ni foams with a nominal porous diameter of 600 μm in an AWE zero-gap cell [18]. Recently, also ref. [19] reported a synergetic effect when combining Ni foams with a forced flow. However, what is currently still lacking in the literature is a systematic study on the combining effect of pore size and electrolyte flow rate, in particular under the relatively high flow rates encountered under industrial conditions. As a consequence, the main objective of the current work is to study the electrochemical performance of differently sized pure nickel foams in a zero-gap cell configuration under well-controlled hydrodynamic conditions in a dedicated flow cell. This has allowed for the first time to advance the understanding and interpretation of the influence of their pore size independently from their surface area.

2. Materials and methods

Our experimental setup is illustrated schematically in Fig. 2a. It comprises an anolyte and a catholyte reservoir, both made of 316 l stainless steel, each one connected to a gear pump (PTFE as gear material, produced by Micropump, model GJ-N25. FF3S.A) which creates an upward flow of electrolyte inside the cell. This flow is measured by flow transmitters (Honsberg, model LABO-MID1-I/U/F/C). A 30 wt% KOH (6.9 M) electrolyte is prepared by mixing 450 g of potassium hydroxide pellets (KOH > 85%, VWR chemicals) to 1.05 L of deionized water (18.2 MΩ.cm, Sartorius Arium 611). Since iron impurities in the electrolyte are known to activate the anode [20], samples of the electrolyte were taken before starting the experiment and analyzed with inductively coupled mass spectrometry (ICP-MS). Within a detection limit of 0.01 ppm, no iron was detected. Stirrer hotplates from IKA are placed below the reservoirs to impose a temperature of 70 °C inside the cell. The produced gases are collected in graduated cylinders. The cell contains the following parts: two polytetrafluoroethylene (PTFE) end-plates with fittings for inlet and outlet of electrolyte; a nickel (> 95%) current collector to ensure removal of electrical charge; two 6 mm thick PTFE electrode housings to accommodate the electrodes and promote sealing; a Zirfon Perl UTP 500 diaphragm (500 ± 50 μm of thickness) and a nickel (>95%) current feeder to supply electrical charge. Between each one of these parts, there is a 1 mm ethylene propylene diene monomer (EPDM) layer to ensure sealing and to prevent mechanical wear.

To assess the hydrodynamic behavior of the cell, we performed computational fluid dynamics (CFD) simulations of the fluid flow. The model geometry of the cell was created and meshed using Gmsh [21]. An element size of 0.0005 m was imposed in order to resolve the flow scales

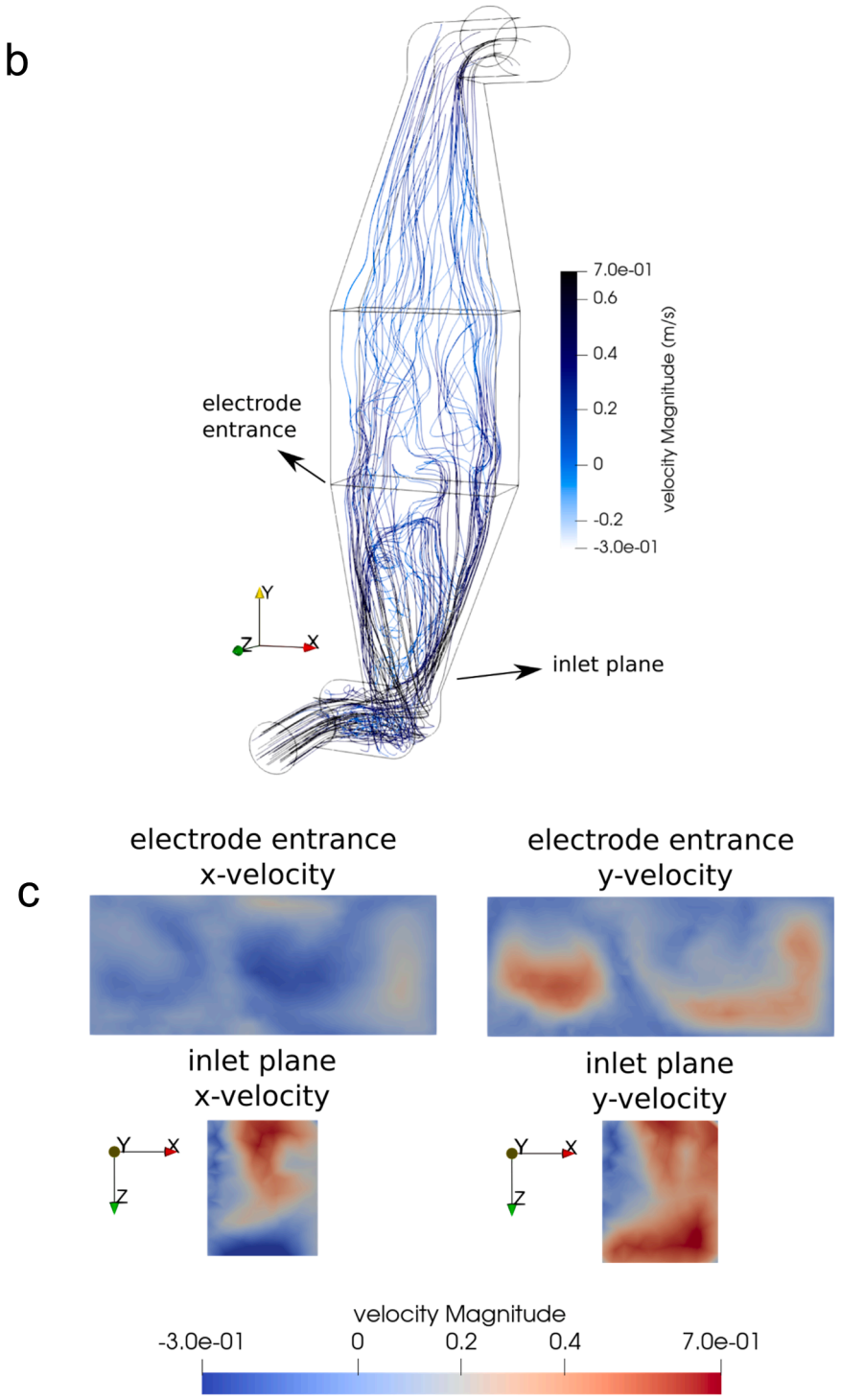

Fig. 2. (*continued*).

of interest. The incompressible Navier-Stokes equations for a single-phase flow were solved using the finite element method (FEM) implemented in MigFlow [22]. For the imposed maximum flow rate of 1.1 L/min through an inlet pipe of radius 3 mm, the inlet velocity of the fluid is calculated at 0.6484 m/s, corresponding to Reynolds number of 4897. We can thus consider that the flow is in the turbulent regime. The flow is simulated through the cell without the presence of an electrode since our main interests in this study are the inlet flow characteristics and the resulting velocity profiles near the electrode entrance. To this end, we have to explore two contradictory objectives. On the one hand, high flow rates and thus high velocities have to be imposed to study the efficiency of bubble removal from the porous electrodes. On the other hand, smooth velocity profiles on the electrode entrance are desired. Since the velocity of the fluid is high in the tubular inlet of small diameter, we can expect the immediate development of flow instabilities. Direct injection of the electrolyte through an inlet of small diameter would develop to a jet stream in the upwards direction. Instead, the double elbow design of our cell inlet guides the flow into a vortical structure, as visualized by the velocity streamline tracing (Fig. 2b). This enhances the spread of electrolyte throughout the cell.

Table 1
Geometrical electrode characteristics.

Measured (Specified) pore size (μm)	Measured (Specified) porosity (%)	Measured (Specified) surface area (cm^2/cm^3)	Number of layers	Measured (Specified) total thickness (cm)	Measured foam surface area per cell (cm^2)
430 ± 60 (450)	87 ± 8 (85)	42.4 (78)	5	0.81 ± 0.02 (0.80)	135.7
500 ± 100 (580)	89 ± 7 (90)	42.8 (69)	4	0.77 ± 0.01 (0.76)	130.1
800 ± 100 (800)	91 ± 5 (90)	34.7 (60)	3	0.75 ± 0.01 (0.75)	104.1
1000 ± 200 (1200)	93 ± 4 (90)	23.2 (43)	2 + 2/3	0.78 ± 0.01 (0.8)	74.2
3500 ± 700 (3000)	95 ± 3 (94)	9.9 (11)	2	0.77 ± 0.03 (0.8)	31.7

Subsequently, the flow cell has been specifically designed with increasing area in the x-z plane as we move towards the electrode entrance. This design helps to homogenize as much as possible the flow. In Fig. 2c we visualize the profiles of the x and y-velocity components on two x-z planes: one after the inlet and one before the electrode. We are mainly interested in the elimination of variations in the x-velocity component since they denote turbulence and mixing of the electrolyte in the x-z plane (the qualitative behaviour of the z-component is similar). These instabilities are eliminated as the flow evolves to the electrode's entrance and therefore the flow is laminarized in the main flow direction of the electrolyte through the electrode.

To prepare the electrodes, sheets of porous nickel foams (>99%) were cut into pieces of 2 × 2 cm^2. These pieces were stacked to fill the 8 mm gap provided by the electrode housing and the EPDM layers. Different pore sizes were studied, ranging from 450 to 3000 μm. Specifications of the nickel foams under investigation are shown in Table 1. In the case of a pore size of 1200 μm, one of the three layers was polished until its thickness reached 0.2 cm. This way, the total electrode thickness was 0.8 cm (2 ×0.3 cm + 0.2 cm). The nickel foams were manufactured by Alantum using an open cell polyurethane (PU) foam as a substrate for nickel sputtering. Then, a 560 °C pyrolysis removed the PU

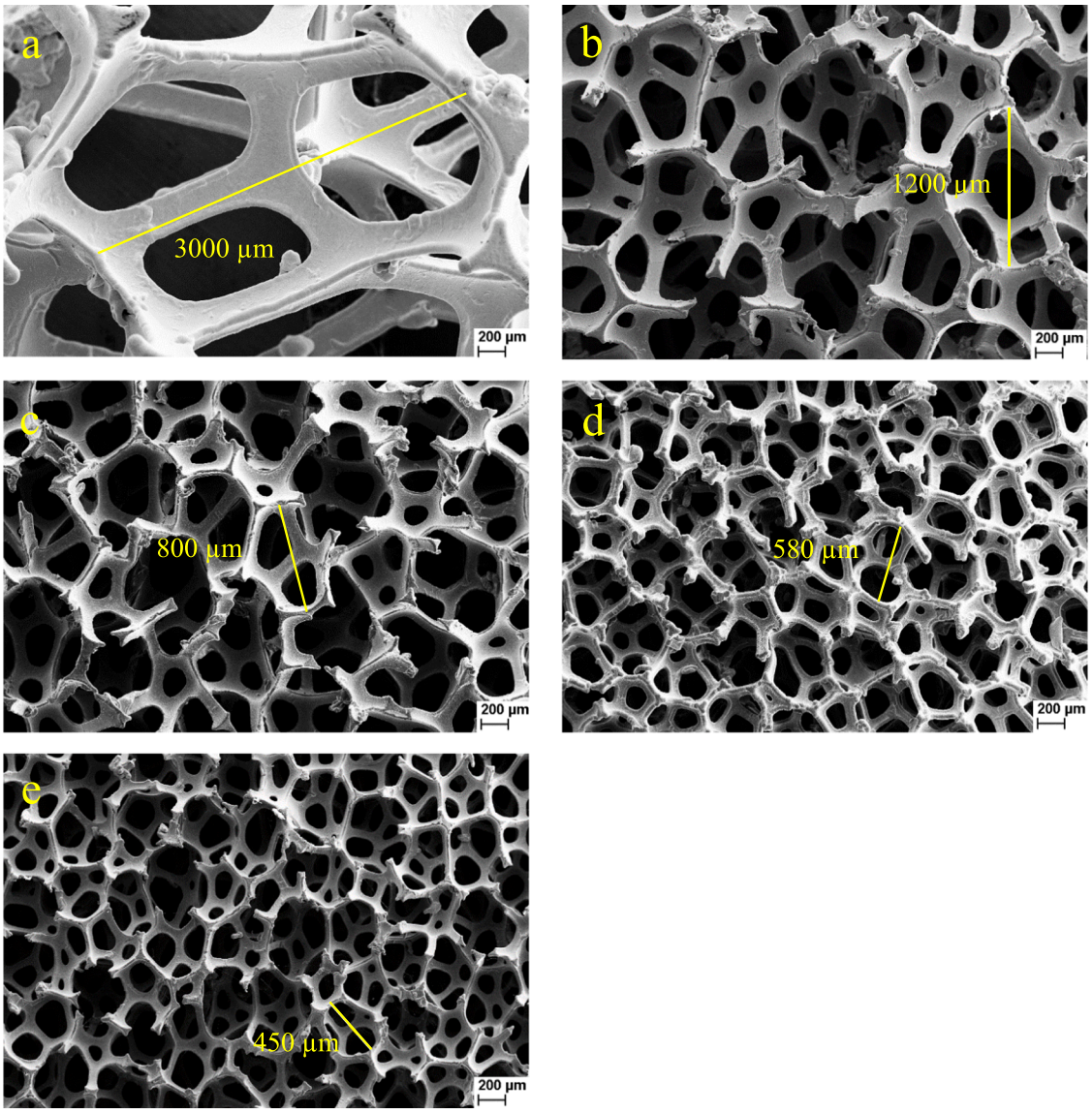

Fig. 3. Scanning electron micrographs taken at the same magnification for porous nickel foams with specified pore sizes of a) 3000 μm b) 1200 μm c) 800 μm d) 580 μm e) 450 μm.

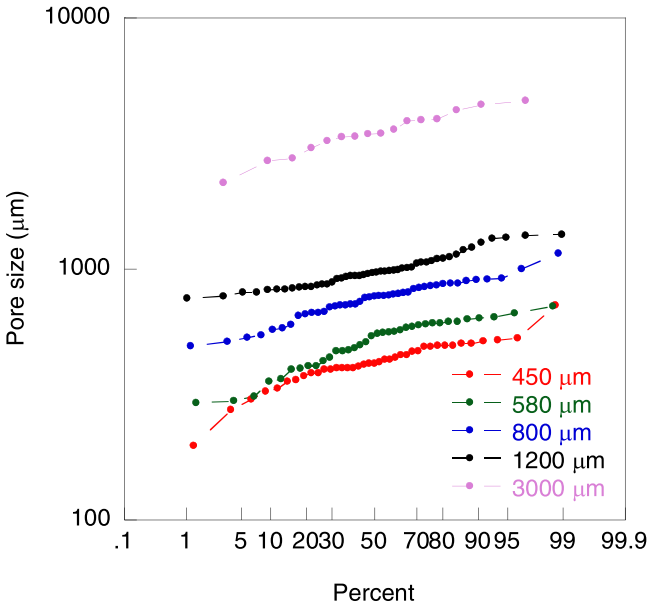

Fig. 4. Probability plot for pore size distribution of foam electrodes.

and subsequently the material was annealed at 950 °C [23]. According to this procedure, a different layer thickness results for each pore size. Therefore, in order to accommodate the differently sized foams into our cell, a different number of layers needs to be used, as indicated in Table 1 as well.

Two experiments were designed to study the electrochemical performance of nickel foams. In the first one, the current was cycled six times from 0 to 2 A at a scan rate of 100 mA/s. This step was followed by 5 galvanostatic experiments of 5 min each at 0.4, 0.8, 1.2, 1.6, and 2.0 A, respectively. Then, the same current cycling as in the beginning was performed. Galvanostatic experiments were chosen because, even though it is time-consuming, a steady-state measurement can effectively remove the background currents caused by capacitive behavior and oxides formation [8]. This experiment was performed for all the nickel foams. A setup without foam, so only with the current collector and the current feeder, was tested as well. The second experiment was designed to compare bubble entrapment inside the electrodes. In that case, two pore sizes were studied: 450 μm and 3000 μm. In that experiment, three pulses of 10 min each were performed: 5 min at 2 A followed by 5 min at zero current. All electrochemical experiments were performed using a Solartron Modulab XM potentiostat. To ensure a temperature of 70 °C inside the electrolytic cell, a hole of 3 mm in diameter was drilled into the electrode housing to insert a thermocouple. In a configuration without electrodes, the temperature at the catholyte reservoir and at the cell interior (cathodic side) was measured. To achieve 70 °C degrees at the cell, a higher temperature needs to be imposed in the reservoir, depending on the electrolyte flow rate. The results obtained in this test were used to impose the right temperature at the reservoir tanks in a way to fix the cell temperature at 70 °C for all the flow rates. The difference in temperature between the reservoir and the cell was in the range of 0.2–2.6 °C, depending on the imposed flow rate. When no forced flow was imposed, the temperature inside the cell decreased rapidly. For instance, during the 25 min needed for the first experimental protocol described above, the decrease in temperature was in the order of 30 °C. This is why in the case of natural convection, only the sixth CV will be used to characterize the electrochemical performance and to compare with the cases where a forced flow was imposed. After this analysis of cell temperature, the thermocouple was removed from the cell, the electrode housing was changed by the one without a hole and the electrochemical experiments were carried out.

Representative micrographs of the foam electrodes, shown in Fig. 3, were taken using a scanning electron microscope (SEM) at an electron high tension of 15 kV and a magnification of 30x. These images were also used to estimate the average pore size of each foam and its standard deviation, as shown in Table 1 as well, while the full pore size distributions are shown in Fig. 4. Outliers were removed in order to better estimate the pore size. Even though there is an overlap between the different foams, z-tests were performed and with an alpha of 0.05, the distributions were proven to be statistically different. The foam thickness was verified using a digital caliper and the porosity was verified by measuring the dislocated volume of water [P = (1-volume dislocated)/(total volume)] [24]. The result for the total porous transport layer thickness shown in Table 1 is an average for the cathode and the anode. Four measurements were done in different locations for each electrode. For the porosity measurement, a geometric surface area of 22 cm^2 of nickel foam was immersed in a graduated cylinder with a precision of

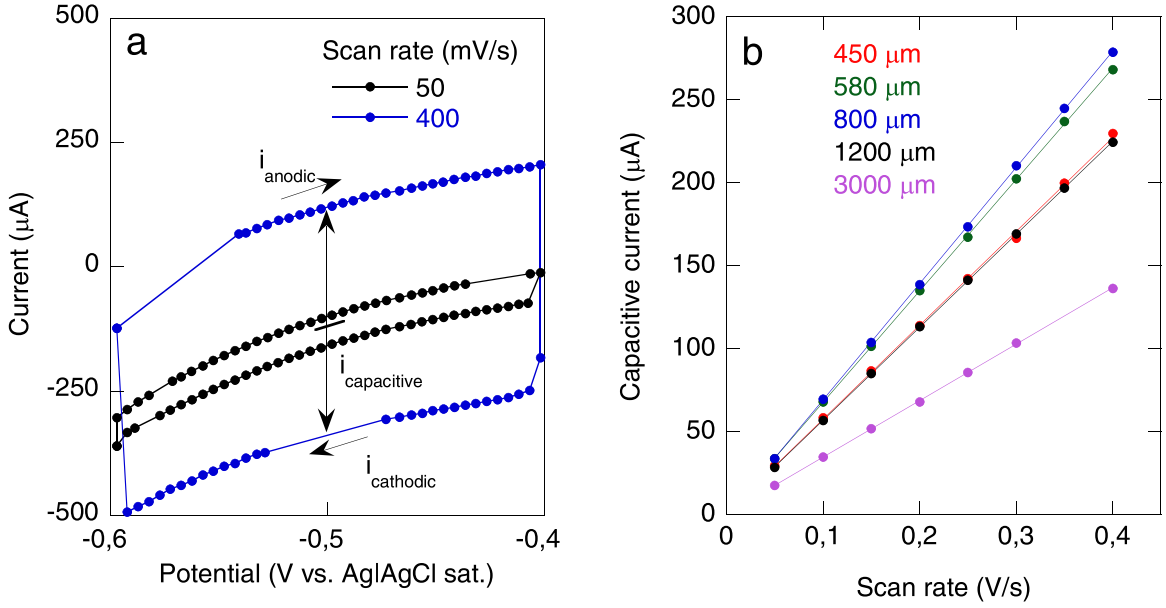

Fig. 5. a) Cyclic voltammetry from − 0.6 V *vs.* Ag=AgCl sat. to − 0.4 V *vs.* Ag|AgCl sat. at scan rates between 50 mV/s and 400 mV/s for one 2 × 2 cm^2 layer of nickel foam with a pore size of 450 μm; b) Resulting capacitive current as a function of scan rate. Experiments were performed at 1 M KOH, room temperature.

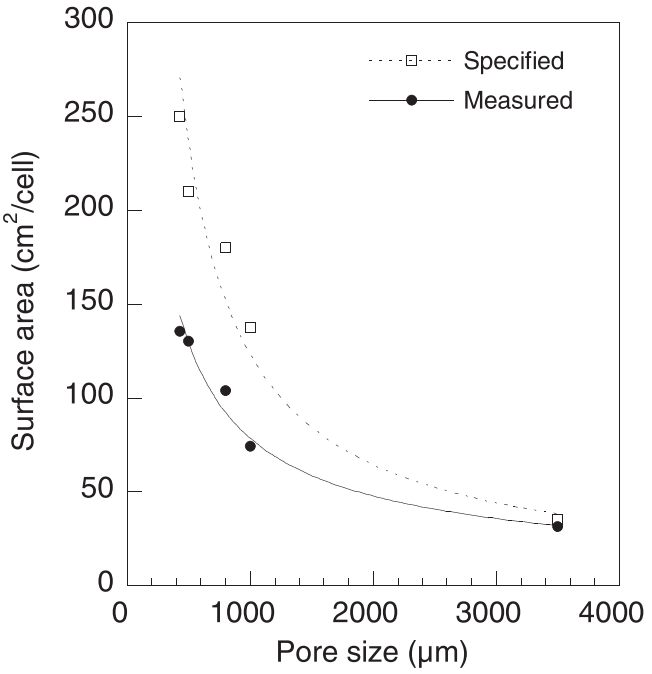

Fig. 6. Specified and measured foam surface area per cell, as a function of measured average pore size.

± 0.25 ml. As shown in Table 1, the expected value was in the range of the measured value as well.

The determination of ECSA was done by measuring the capacitance and considering a specific capacitance of 20 μF/cm^2. The capacitance was calculated by scanning the potential from − 0.6 to − 0.4 V vs Ag|AgCl *sat.* at different scanning rates. The rates went from 50 mV/s to 400 mV/s in steps of 50 mV/s. Three cycles were performed for each scan rate. At this potential range, no reaction occurs (the OCP is around −0.5 V *vs.* Ag|AgCl sat.), but there was the charge and discharge of the electric double layer. When the potential goes from − 0.6 to − 0.4 V *vs.* Ag|AgCl sat. the electrical double layer discharges. When the voltage returns to − 0.6 V *vs.* Ag|AgCl sat. coming from − 0.4 *vs.* Ag|AgCl sat. the electrical double layer is charged. The first current will be called anodic current and the latter the cathodic current. Half of the difference between these currents at − 0.5 V *vs.* Ag|AgCl sat. gives the capacitive current at a certain scan rate. A typical plot for the 2 extreme scan rates is shown in Fig. 5.a. The faster the scan rate, the higher this current will be. The slope of the capacitive current (μA) vs scan rate (V/s) gives the capacitance of the electrode (μF), according to the following equation:

$$\text{Slope} = C_{dl} \quad [\mu F] = \frac{\Delta i_c [\mu A]}{\Delta v [V/s]} \tag{2}$$

with C_{dl} the double layer capacitance, i_c the capacitive current, and v the scan rate. Fig. 5.b shows that there was a linear relation between the capacitive current and the scan rate, what allow us to use the Eq. 2. To reduce the experimental error on the electrode capacitance, the experiment was repeated for each electrode by increasing the number of layers from 1 to 5. The slope of the capacitance vs. the number of layers then gives a better approximation of the one-layer capacitance. The capacitance method was chosen following the conclusion of ref. [25] that this method presents a good correlation with the real surface value even in the presence of nickel oxides. Once the capacitance is estimated, the following correlation holds between the electrode capacitance and its total surface area:

$$A_{ECSA} = \frac{C_{dl}}{c} \tag{3}$$

where c is the specific capacitance. The value of 20 μF/cm^2 is based on previous studies [26–28]. Our setup for this test consists of a three-electrode cell with Pt 110 as the counter-electrode, a saturated Ag|AgCl reference electrode (XR300 from Radiometer Analytical) and the 2 × 2 cm nickel foam as the working electrode. The solution is 1 M of KOH at room temperature, with the same specifications as before.

3. Results and discussion

3.1. Effect of pore size on electrochemically active surface area (ECSA)

In what follows, current densities will be presented either as geometric or electrochemical ones. Geometric current density (j_{GEO}) is the total current divided by the projected area of the electrode (4 cm^2 in this work), while electrochemical current density (j_{ECSA}) is the total current divided by the actual electrochemically active surface area (ECSA). Although values for the electrode specific surface area (in cm^2/cm^3) as a function of pore size have been specified by the manufacturer (as shown in Table 1), a capacitance test was performed to measure the electrochemically active surface area independently. As shown in Fig. 6, the measured specific ECSA is systematically lower than the specified value. This can be due to inhomogeneities in the electrode inherent to the fabrication method, which deviates the value from the specified one. Alternatively, the value of 20 μF/cm^2 assumed for the specific capacitance may not be the most suitable for our setup. The slope of a curve capacitance vs specified surface area gives a specific capacitance of 11.6 ± 0.6 μF/cm^2 setting the intercept to zero and 8.6 ± 1.4 μF/cm^2 with a non-zero intercept. Applying the same method to the current distributor plate, one has an ECSA of 19 cm^2. When estimating the ECSA current density, shown in Fig. 7, this value was also considered.

The capacitance method is a good way to compare electrochemical active surface areas, but the estimation of the exact value is difficult as it depends on the value chosen for the specific capacitance. There is no consensus in the literature about this value, as experiments are conducted in different conditions and setups. Not all Ni electrodes in the literature are the same: they have different purities and different oxides content. Furthermore, the surface area is often estimated differently. While some articles consider the geometrical surface area, others use the BET surface area. Even for polished Ni electrodes, as in ref. [29], a difference in specific capacitance was observed when considering the geometric surface area of a polished and an etched electrode. Moreover, the electrode holder used to make the electric contact of the nickel electrode, if immersed, will also present a capacitance and will alter the result. If the electrode holder is not immersed it means that the foam will be partially immersed. In this case, the capillary effect in foams will increase the area in contact with the solution and alter the results. Differences in thickness, porosity and density will change the wicking height and in turn the apparent ECSA, making it harder to compare between different studies [30]. This is why it was strictly important here to follow the same protocol to have a good ECSA comparison, with electrodes fully immersed. The effect of the electrode holder was greatly reduced here as the one-foam ECSA value was estimated from the slope of the curve capacitance vs number of layers, with the intercept representing the capacitance of the holder.

3.2. Effect of pore size on the electrochemical performance

When looking at the cell-voltage values obtained at a fixed geometric current density (Fig. 8), it can be seen that the use of nickel foams enhances hydrogen production as compared to the case where only a 2D current distributor plate was used. At 0.5 A/cm^2 one has a decrease between 200 and 400 mV in cell voltage, representing a 15–30% decrease in overpotential (i.e. the cell voltage minus 1.23 V), for both natural convection and forced electrolytic flow. This means that even if bubbles get trapped inside the foam internal structure, hydrogen

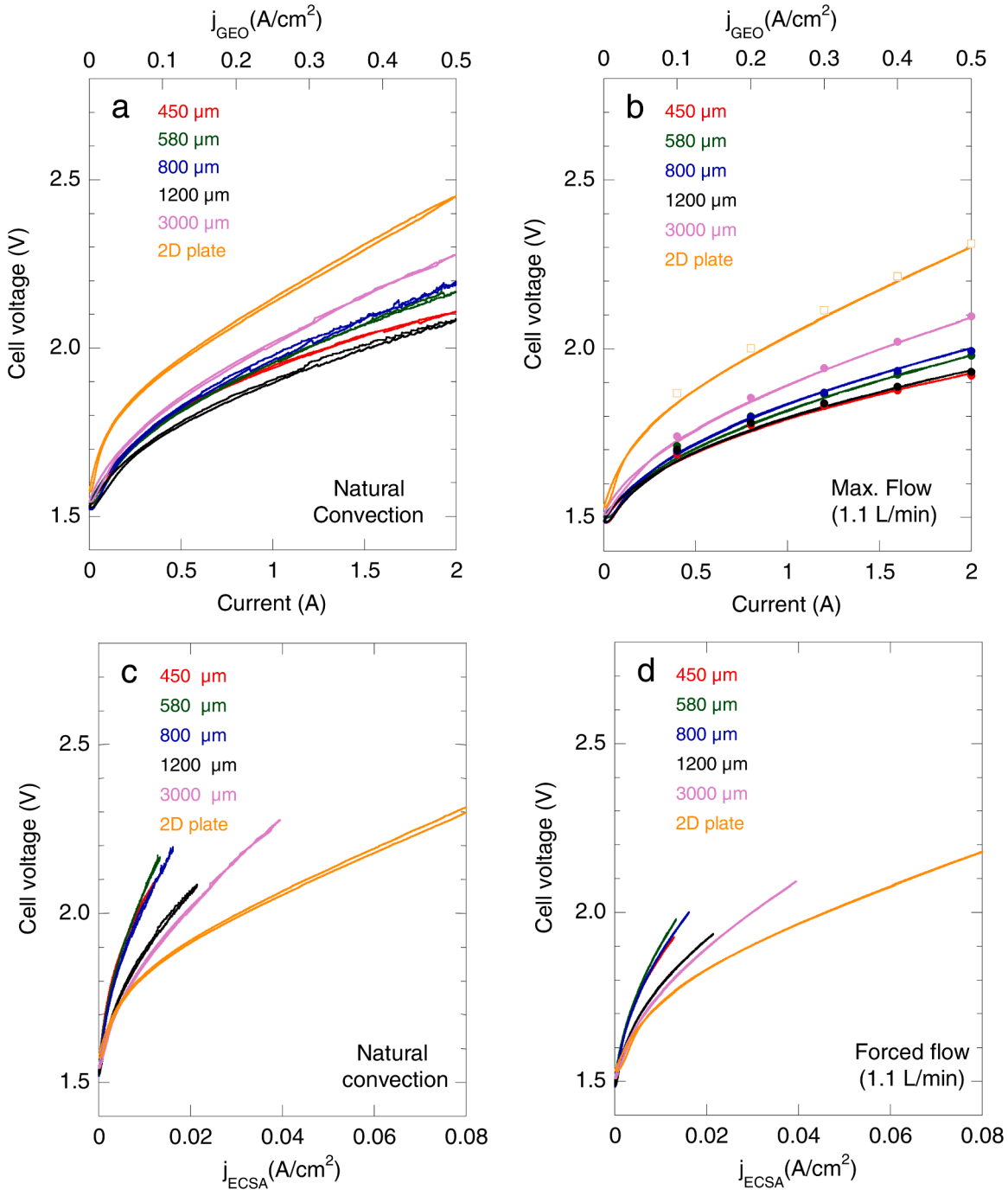

Fig. 7. Cell voltage as a function of a) geometrical current density during natural convection; b) geometric current density for a flow rate of 1.1 L/min; c) electrochemical current density at natural convection; d) electrochemical current density at a flow rate of 1.1 L/min. Lines represent the results of CV scans at 100 mA/s, while the additional symbols in b) represent the mean cell voltage during a 5 min galvanostatic stay. All experiments were performed at 30% KOH and 70 °C.

production can still benefit from the higher surface area offered by the foams and by the lower interelectrode gap. This result shows the advantage of the zero-gap design over the traditional design.

As illustrated in Fig. 8, the presence of a forced flow promotes a further decrease in cell voltage, between 40 and 100 mV at 0.1 A/cm^2 and between 120 and 190 mV at 0.5 A/cm^2, dependent on the pore size. This represents a significant decrease of up to 20% in overpotential.

No clear trend can be observed in Fig. 7a and Fig. 7b as to the effect of pore size on the flow-induced performance improvement. The best pore sizes are 450 µm and 1200 µm, as they promote the highest geometric current densities at a fixed cell voltage. At this stage, we might speculate already that the 450 µm foam presents a good performance due to its high surface area of 135.7 cm^2, while the 1200 µm foam benefits from a better bubble removal efficiency, even if its surface area is lower (74.2 cm^2). The average cell voltage for every 5 min galvanostatic experiment - represented by the additional symbols in Fig. 7b - shows a good agreement with the results from the cyclic voltammetry. The voltage is slightly higher at a fixed current for the galvanostatic one as a consequence of the higher time of the experiment, which allows the full development of the diffusional layer and therefore enhances bubble entrapment. Looking at the cell voltage at which the current starts to increase, an offset is observed in the case when no foam was used. This offset is pore size dependent, 50 mV being the maximum value observed in the case of the smallest sized (450 µm) pores. For the biggest pore

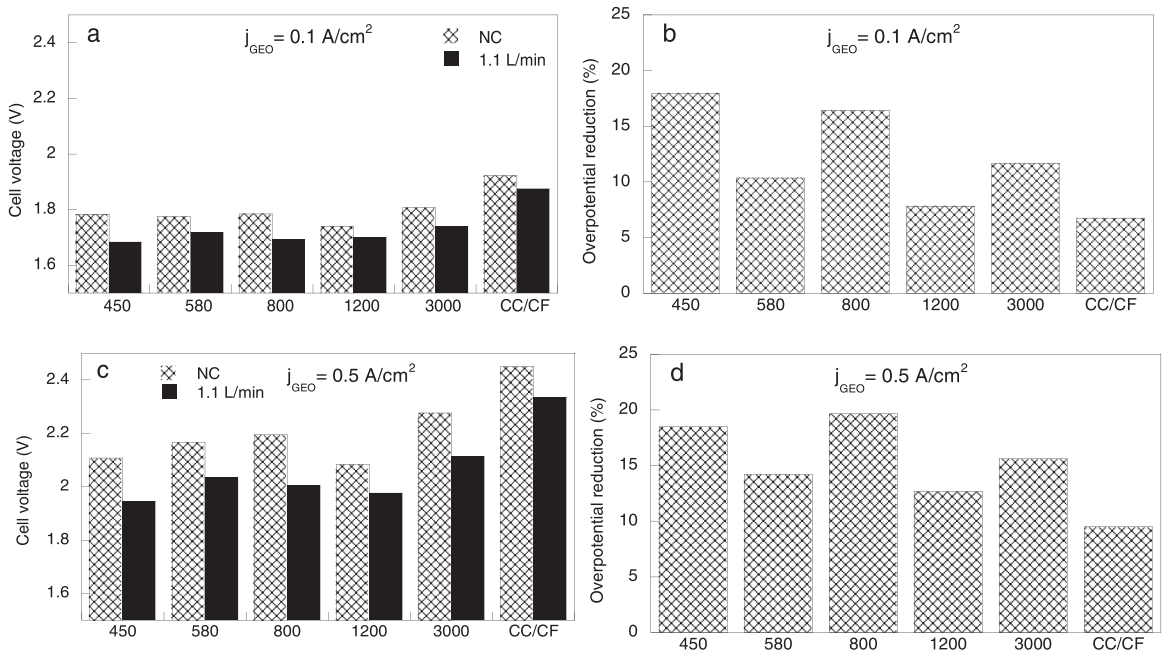

Fig. 8. Cell voltage for the different foams and flow regimes at a) 0.1 A/cm^2 and c) 0.5 A/cm^2. Percentage reduction in cell voltage caused by a forced electrolytic flow (1.1 L/min) at b) 0.1 A/cm^2 and d) 0.5 A/cm^2.

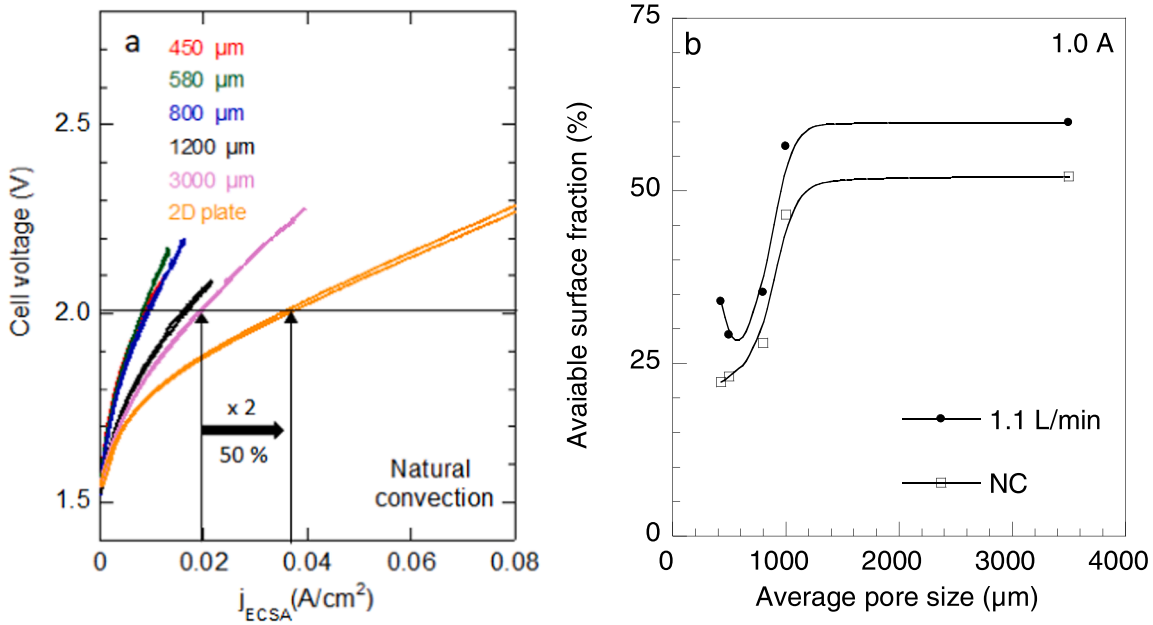

Fig. 9. a) Illustration of the method for calculating the available surface fraction for a foam electrode; b) Fraction of available surface area as a function of measured average pore size at 1 A under natural convection and 1.1 L/min. Solid rend lines are merely a guide to the eye.

sizes (3000 µm), the offset reduces to about 30 mV. In other words, the observed offset for the 2D Ni sheet cannot only be attributed to the higher Ohmic drop related to the higher interelectrode distance.

Interestingly, the effect of pore size becomes much more systematic when expressing the cell voltage vs. electrochemical current density j_{ECSA} (Fig. 7c and Fig. 7d). It can be seen that the highest current densities were achieved when no foam was used. Then, higher pore sizes presented systematically the highest j_{ECSA} values. Since all the electrodes were made of pure nickel, the electrochemical performance normalized by the ECSA should be the same. In other words: all curves in Fig. 7c and d should in principle superimpose. The observed decrease in j_{ECSA} with smaller pore size can therefore be attributed to bubble entrapment. This decreases the fraction of effectively active surface area, thereby giving the impression of a worse electrochemical activity. It is logical then that the smaller the pore size, the higher the risk of bubble entrapment. To estimate the fraction of effectively available surface area relative to the theoretically available ECSA values shown in Fig. 6, we propose a new procedure that is illustrated in Fig. 9a. It is based on comparing the 3D foam's electrochemical current density at a fixed cell voltage to the j_{ECSA} value of the 2D nickel plate. The fraction of available surface area can then be calculated as the ratio between the current density for each foam divided by the current density without foam, following Eq. 2. Indeed, the position of the foam's polarization curve to the left of the one for a 2D plate when normalizing by the theoretical ECSA value implies that

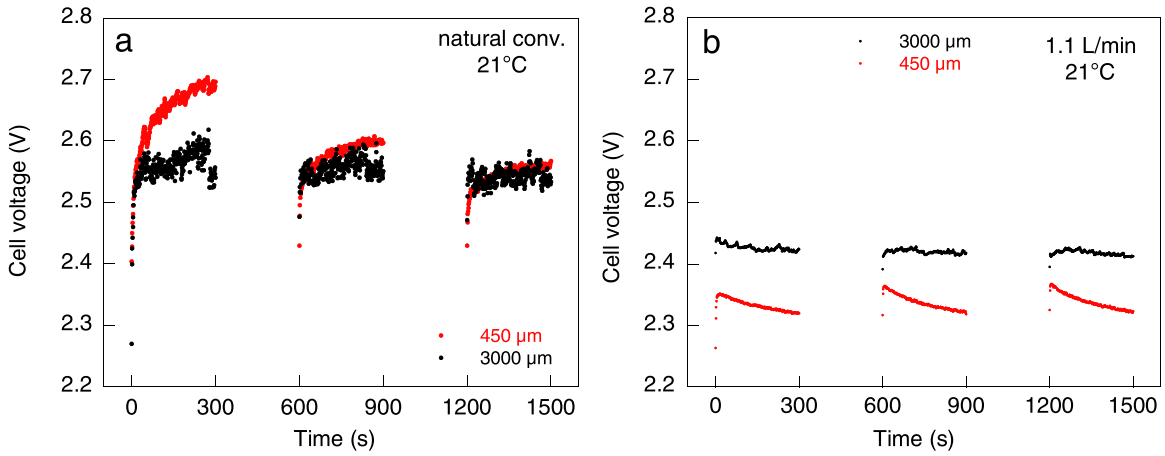

Fig. 10. Evolution of cell voltage for three series of galvanostatic pulses of 5 min at a geometric current density of 0.5 A/cm^2 followed by 5 min at zero current; a) natural convection b) 1.1 L/min. Experiments were performed at 30 wt% KOH and room temperature.

we have divided the total current by a too high value for the effectively available surface area. The latter fraction can thus be calculated by the correction factor needed to make both curves superimpose. The results are shown in Fig. 9b for the case of natural convection and maximum flow. It clearly confirms that the lower the pore size, the lower the percentage of available surface. At 1.0 A and natural convection, one has 52% of available surface for 3000 µm and only 22% for 450 µm. A qualitatively similar effect was observed at the maximum flow rate, going from 60% for 3000 µm to 34% for 450 µm. This result also demonstrates that a forced electrolytic flow increases the surface availability, especially for the lowest pore size. For the latter, an increase in surface availability in the order of 53% was observed, while the others presented an increase between 15% and 26%.

One must note that the above results are drawn with no IR correction on the polarization curve of the 2D reference plate. The correction is very challenging, as it makes our analysis physically impossible at technology relevant voltages. Although a more rigorous analysis would require to apply such a correction, it is unfortunately not possible here.

What can be concluded from all the above is that, when selecting the most appropriate pore size, there is a compromise between surface area and bubble removal efficiency. Since in the case of foams a larger surface area intrinsically implies a smaller pore size and a higher bubble entrapment, there should indeed be an optimum. Here, it was observed that for all the pore sizes studied, it can be interesting to maximize the surface area using a relatively small pore size of 450 µm, but it can also be interesting to enhance the bubble removal efficiency by the use of a more open structure, such as a 1200 µm sized foam, compensating for its lesser surface area.

3.3. *Effect of pore size on bubble entrapment*

In an effort to confirm the hypothesis of bubble entrapment, we compared the foam with the best performance (450 µm) to the one with the worst performance (3000 µm) during three galvanostatic series of 5 min at 0.5 A/cm^2 (geometric current density) followed by a current off period of 5 min, both at natural convection and forced flow. As described in [32], during such pulsed experiments, the off-period provides time for bubble removal and recovery of any surface area that was blocked by the bubbles. However, if the bubbles are confined and cannot be removed, the cell potential will increase after each on period due to blockage of the electrode surface by bubbles and the resulting loss of active surface area. In order to ensure the same temperature inside the cell and knowing the existence of a temperature decay at natural convection, this experiment was done at room temperature (21 °C). The result is shown in Fig. 10. At natural convection, the cell voltage increases with time as a consequence of an increase in bubble entrapment, which gradually reduces the active surface area. As expected, this increase is higher for the lowest pore size, as more bubbles are getting trapped within the 3D structure. The cell voltage increase for the 450 µm foam becomes less and less significant during the 3 consecutive cycles. We speculate that there might have been some residual air bubbles inside the 450 µm foam at the start of the experiment. During the first off-time period, these bubbles could then leave the structure. At a flow rate of 1.1 L/min, no significant increase in cell voltage was observed, which demonstrates that at this flow rate, bubble removal was effective. In this case, after a short period of cell voltage increase, there was even a decay in cell voltage, especially for the 450 µm foam. This result confirms the importance of a forced electrolytic flow in removing bubbles and avoiding cell voltage build-up. Also note that much more pronounced fluctuations in the cell voltage evolution are observed at natural convection than under forced electrolyte flow. This is partly because of more important bubble entrapment, but also because of a more inhomogeneous temperature profile within the electrolyte, leading to density fluctuations and hence a gradient in buoyancy forces. Finally, at natural convection, the foam with a pore size of 450 µm even presented a performance which is slightly worse than the foam with a pore size of 3000 µm. In other words, it only makes sense to use small-sized foams if a forced electrolyte flow is imposed, otherwise, bubbles cannot leave the electrode surface.

4. Conclusion

In conclusion, the zero-gap design has proven to be more performant than the traditional cell, causing a 400 mV reduction in cell voltage at 0.5 A/cm^2. Furthermore, the choice of a porous transport layer depends mainly on two opposing factors: surface area and bubble entrapment. To increase surface area, the pore size should be reduced. On the other hand, this will increase bubble entrapment and hinder hydrogen production. When looking at the ECSA current density, it was clear that more closed structures with lower pore sizes caused a decrease in the observed current density. This was mainly a consequence of a higher bubble entrapment. From all the foams studied, the best compromise between surface area and bubble entrapment was found for 450 µm and 1200 µm. For the first one, it makes sense to choose this pore size only when a forced electrolyte flow is imposed. Otherwise, bubble entrapment is too significant and the performance decreases. The electrolytic flow has proven to be promising, promoting a decrease in overpotential of up to 20%. Furthermore, while pores of 450 µm benefit from the highest surface area, pores of 1200 µm benefit from a more open structure responsible for better bubble removal. From a technological point of view, electrolyzer manufacturers should choose between the drawback of smaller electrode structures – where a higher forced

electrolyte flow is needed - and more open electrode structures – where a higher cell stack volume is needed. A recommendation for the following studies is to create and analyze special structures which can improve bubble removal while keeping the surface area at a maximum value. With 3-D printing technologies, there is an infinity of possible structures to be studied.

Declaration of Competing Interest

The authors declare that they have no known competing financial interests or personal relationships that could have appeared to influence the work reported in this paper.

Acknowledgments

We gratefully acknowledge financial support from the European Commission, Belgium, through the Horizon 2020 Project "NexTAEC" (Materials for Next Generation Alkaline Electrolyzers), under contract n° 862509.

References

[1] M. Götz, J. Lefebvre, F. Mörs, A. McDaniel Koch, F. Graf, S. Bajohr, R. Reimert, T. Kolb, Renewable power-to-gas: a technological and economic review, Renew. Energy 85 (2016) 1371–1390, https://doi.org/10.1016/j.renene.2015.07.066.
[2] R.-H. Lin, Y.-Y. Zhao, B.-D. Wu, Toward a hydrogen society: hydrogen and smart grid integration, Int. J. Hydrog. Energy 45 (2020) 20164–20175, https://doi.org/10.1016/j.ijhydene.2020.01.047.
[3] R.L. LeRoy, Industrial water electrolysis: present and future, Int. J. Hydrog. Energy 8 (1983) 401–417, https://doi.org/10.1016/0360-3199(83)90162-3.
[4] S.A. Grigoriev, V.N. Fateev, D.G. Bessarabov, P. Millet, Current status, research trends, and challenges in water electrolysis science and technology, Int. J. Hydrog. Energy 45 (2020) 26036–26058, https://doi.org/10.1016/j.ijhydene.2020.03.109.
[5] S. Shiva Kumar, V. Himabindu, Hydrogen production by PEM water electrolysis – a review, Mater. Sci. Energy Technol. 2 (2019) 442–454, https://doi.org/10.1016/j.mset.2019.03.002.
[6] R. Phillips, C.W. Dunnill, Zero gap alkaline electrolysis cell design for renewable energy storage as hydrogen gas, RSC Adv. 6 (2016) 100643–100651, https://doi.org/10.1039/C6RA22242K.
[7] M. Schalenbach, O. Kasian, K.J.J. Mayrhofer, An alkaline water electrolyzer with nickel electrodes enables efficient high current density operation, Int. J. Hydrog. Energy 43 (2018) 11932–11938, https://doi.org/10.1016/j.ijhydene.2018.04.219.
[8] T. Kou, S. Wang, Y. Li, Perspective on high-rate alkaline water splitting, ACS Mater. Lett. 3 (2021) 224–234, https://doi.org/10.1021/acsmaterialslett.0c00536.
[9] G.B. Darband, M. Aliofkhazraei, S. Shanmugam, Recent advances in methods and technologies for enhancing bubble detachment during electrochemical water splitting, Renew. Sustain. Energy Rev. 114 (2019), 109300, https://doi.org/10.1016/j.rser.2019.109300.
[10] T. Kou, S. Wang, R. Shi, T. Zhang, S. Chiovoloni, J.Q. Lu, W. Chen, M.A. Worsley, B. C. Wood, S.E. Baker, E.B. Duoss, R. Wu, C. Zhu, Y. Li, Periodic porous 3D electrodes mitigate gas bubble traffic during alkaline water electrolysis at high current densities, Adv. Energy Mater. 10 (2020), 2002955, https://doi.org/10.1002/aenm.202002955.
[11] J. Parra-Restrepo, R. Bligny, J. Dillet, S. Didierjean, D. Stemmelen, C. Moyne, A. Degiovanni, G. Maranzana, Influence of the porous transport layer properties on the mass and charge transfer in a segmented PEM electrolyzer, Int. J. Hydrog. Energy 45 (2020) 8094–8106, https://doi.org/10.1016/j.ijhydene.2020.01.100.
[12] J.-H. Kim, J.-N. Lee, C.-Y. Yoo, K.-B. Lee, W.-M. Lee, Low-cost and energy-efficient asymmetric nickel electrode for alkaline water electrolysis, Int. J. Hydrog. Energy 40 (2015) 10720–10725, https://doi.org/10.1016/j.ijhydene.2015.07.025.
[13] W.-B. Han, I.-S. Kim, M. Kim, W.C. Cho, S.-K. Kim, J.H. Joo, Y.-W. Lee, Y. Cho, H.-S. Cho, C.-H. Kim, Directly sputtered nickel electrodes for alkaline water electrolysis, Electrochim. Acta 386 (2021), 138458, https://doi.org/10.1016/j.electacta.2021.138458.
[14] M.R. Kraglund, M. Carmo, G. Schiller, S.A. Ansar, D. Aili, E. Christensen, J. O. Jensen, Ion-solvating membranes as a new approach towards high rate alkaline electrolyzers, Energy Environ. Sci. 12 (2019) 3313–3318, https://doi.org/10.1039/C9EE00832B.
[15] S. Abdelghani-Idrissi, N. Dubouis, A. Grimaud, P. Stevens, G. Toussaint, A. Colin, Effect of electrolyte flow on a gas evolution electrode, Sci. Rep. 11 (2021) 4677, https://doi.org/10.1038/s41598-021-84084-1.
[16] R. Phillips, C. Dunnill, Zero Gap Cell Des. Alkaline Electro, 2019 doi: 10.13140/RG.2.2.26663.29606.
[17] E. Amores, J. Rodríguez, J. Oviedo, A. de Lucas-Consuegra, Development of an operation strategy for hydrogen production using solar PV energy based on fluid dynamic aspects, Open Eng. 7 (2017) 141–152, https://doi.org/10.1515/eng-2017-0020.
[18] A. Đukić, M. Firak, Hydrogen production using alkaline electrolyzer and photovoltaic (PV) module, Int. J. Hydrog. Energy 36 (2011) 7799–7806, https://doi.org/10.1016/j.ijhydene.2011.01.180.
[19] A. Kovač, D. Marciuš, L. Budin, Solar hydrogen production via alkaline water electrolysis, Int. J. Hydrog. Energy 44 (2019) 9841–9848, https://doi.org/10.1016/j.ijhydene.2018.11.007.
[20] M.R. Kraglund, D. Aili, K. Jankova, E. Christensen, Q. Li, J.O. Jensen, Zero-gap alkaline water electrolysis using ion-solvating polymer electrolyte membranes at reduced KOH concentrations, J. Electrochem. Soc. 163 (2016) F3125–F3131, https://doi.org/10.1149/2.0161611jes.
[21] C. Geuzaine, J.-F. Remacle, Gmsh: A 3-D finite element mesh generator with built-in pre- and post-processing facilities, Int. J. Numer. Methods Eng. 79 (2009) 1309–1331, https://doi.org/10.1002/nme.2579.
[22] M. Constant, F. Dubois, J. Lambrechts, V. Legat, Implementation of an unresolved stabilised FEM–DEM model to solve immersed granular flows, Comput. Part. Mech. 6 (2019) 213–226, https://doi.org/10.1007/s40571-018-0209-4.
[23] K. Oh, E. Lee, J.S. Bae, M. Jang, R. Poss, B. Kieback, G. Walthe, B. Kloeden, Large scale production and applications of alloy metal foam, Proc. 7th Int. Conf. Porous Met. Met. Foam. MetFoam, 2011.
[24] S.P. Zankowski, P.M. Vereecken, Electrochemical determination of porosity and surface area of thin films of interconnected nickel nanowires, J. Electrochem. Soc. 166 (2019) D227–D235, https://doi.org/10.1149/2.0311906jes.
[25] E. Cossar, M.S.E. Houache, Z. Zhang, E.A. Baranova, Comparison of electrochemical active surface area methods for various nickel nanostructures, J. Electroanal. Chem. 870 (2020), 114246, https://doi.org/10.1016/j.jelechem.2020.114246.
[26] J. van Drunen, B. Kinkead, M.C.P. Wang, E. Sourty, B.D. Gates, G. Jerkiewicz, Comprehensive structural, surface-chemical and electrochemical characterization of nickel-based metallic foams, ACS Appl. Mater. Interfaces 5 (2013) 6712–6722, https://doi.org/10.1021/am401606n.
[27] J.L. Weininger, M.W. Breiter, Hydrogen evolution and surface oxidation of nickel electrodes in alkaline solution, J. Electrochem. Soc. 111 (1964) 707, https://doi.org/10.1149/1.2426216.
[28] A. Lasia, A. Rami, Kinetics of hydrogen evolution on nickel electrodes, J. Electroanal. Chem. Interfacial Electrochem. 294 (1990) 123–141, https://doi.org/10.1016/0022-0728(90)87140-F.
[29] M. Grdeń, M. Alsabet, G. Jerkiewicz, Surface science and electrochemical analysis of nickel foams, ACS Appl. Mater. Interfaces 4 (2012) 3012–3021, https://doi.org/10.1021/am300380m.
[30] W. Zheng, M. Liu, L.Y.S. Lee, Best practices in using foam-type electrodes for electrocatalytic performance benchmark, ACS Energy Lett. 5 (2020) 3260–3264, https://doi.org/10.1021/acsenergylett.0c01958.
[32] F. Yang, M.J. Kim, M. Brown, B.J. Wiley, Alkaline water electrolysis at 25 A cm-2 with a microfibrous flow-through electrode, Adv. Energy Mater. (2020), 2001174.